Lateral and Vertical Two-Dimensional Layered Topological Insulator Heterostructures

Yanbin Li,[†] Jinsong Zhang,[†] Guangyuan Zheng,[†] Yongming Sun,[†] Seung Sae Hong,[‡] Feng Xiong,[†] Shuang Wang,[§] Hye Ryoung Lee,[§] and Yi Cui*[,†,∥]

[†]Department of Materials Science and Engineering, [‡]Department of Applied Physics, and [§]Department of Electrical Engineering, Stanford University, Stanford, California 94305, United States and [∥]Stanford Institute for Materials and Energy Sciences, SLAC National Accelerator Laboratory, 2575 Sand Hill Road, Menlo Park, California 94025, United States

ABSTRACT The heterostructured configuration between two-dimensional (2D) semiconductor materials has enabled the engineering of the band gap and the design of novel devices. So far, the synthesis of single-component topological insulator (TI) 2D materials such as Bi_2Se_3, Bi_2Te_3, and Sb_2Te_3 has been achieved through vapor phase growth and molecular beam epitaxy; however, the spatial controlled fabrication of 2D lateral heterostructures in these systems has not been demonstrated yet. Here, we report an *in situ* two-step synthesis process to form TI lateral heterostructures. Scanning transmission electron microscopy and energy-dispersive X-ray mapping results show the successful spatial control of chemical composition in these as-prepared heterostructures. The edge-induced growth mechanism is revealed by the *ex situ* atomic force microscope measurements. Electrical transport studies demonstrate the existence of p−n junctions in Bi_2Te_3/Sb_2Te_3 heterostructures.

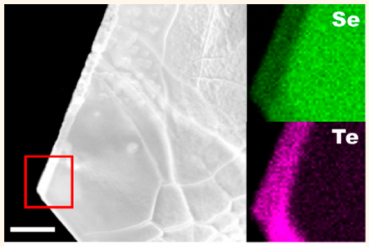

Bi_2Te_3/Bi_2Se_3 Lateral Heterostructure

KEYWORDS: lateral heterostructures · layered materials · topological insulator · *in situ* synthesis method · electrical transport measurements

Heterostructures of two-dimensional (2D) layered materials have emerged as a family of materials that exhibit many interesting physical properties.[1−8] As 2D materials, group V−VI topological insulators (TIs) Bi_2Se_3, Bi_2Te_3, and Sb_2Te_3 show new states of quantum matter. TIs have an insulating gap in the bulk and gapless helical surface states, which means the electron spin is locked perpendicular to momentum.[9−13] This helical property results in the suppression of electron backscattering from crystal defects and nonmagnetic impurities as long as the time-reversal symmetry is preserved.[14−16] As shown in Figure 1a, lateral heterostructures are constructed by adjoined heterogeneous layered materials along the intraplane direction, different from vertical heterostructures, in which two layered materials are stacked along the interplane direction.[7] While vertical TI heterostructures has been studied[17,18] and purposed as a candidate to observe topological exciton condensation,[19] theoretical works show that TI lateral p−n heterostructures have a gapless chiral edge state along the interface in the presence of an external magnetic field[20] and can further serve as a spin filter.[21] Exploring the potential of TI lateral heterostructures will open up a new route to novel electronics and spintronics. Although two-dimensional lateral heterostructures have been first reported between graphene−boron nitride[2−4] and recently achieved in a transition-metal dichalcogenide system,[5−7] the growth of lateral heterostructures between group V−VI TIs remains challenging due to easy formation of an alloy phase.[22] Here, we developed an *in situ* two-step synthesis process to grow TI lateral heterostructures by a vapor−solid growth mechanism. *Ex situ* atomic force microscope (AFM) measurements of the two-step growth of Bi_2Se_3 and Bi_2Te_3 reveal the edge-induced growth mechanism of TI lateral heterostructures. Moreover, conductive AFM measurements show p−n diode rectification in the Bi_2Te_3/Sb_2Te_3 heterostructures, which opens up opportunities for TIs in a range of novel electronics and spintronics.

The layered materials Bi_2Se_3, Bi_2Te_3, and Sb_2Te_3 all possess the same crystal structure with the space group $D_{3d}^5(R\bar{3}m)$. As shown in

* Address correspondence to yicui@stanford.edu (Y. Cui).

Received for review June 30, 2015 and accepted October 15, 2015.

Published online 10.1021/acsnano.5b04068

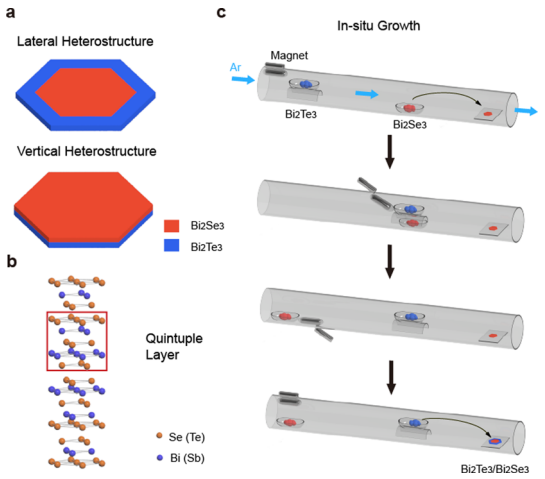

Figure 1. (a) Schematic of a lateral and vertical Bi_2Te_3/Bi_2Se_3 heterostructure. (b) Layered crystal structure of Bi_2Se_3, Bi_2Te_3, and Sb_2Te_3, with each quintuple layer (QL) formed by five Bi (or Sb) and Se (or Te) atomic sheets. (c) Schematic drawing of the *in situ* synthesis process. In the first growth a Bi_2Se_3 (or Sb_2Te_3) boat is put in the center hot zone as the source powder to grow Bi_2Se_3 (or Sb_2Te_3) nanoplates through a vapor−solid growth process. After switching the Bi_2Te_3 boat to the center hot zone, in the second growth, lateral epitaxial growth of Bi_2Te_3 can occur at the edge of the Bi_2Se_3 (or Sb_2Te_3) nanoplates.

Figure 1b, they consist of planar quintuple layers, for example, Se−Bi−Se−Bi−Se in Bi_2Se_3, with a quintuple layer thickness of about 1 nm. The quintuple layers consist of strong intraplanar covalent bonding and are stacked together by weak van der Waals interaction. With this anisotropic bonding, we previously demonstrated the growth of few-layer TI nanoplates on an oxidized silicon surface *via* a vapor−solid (VS) synthesis process.[23] Furthermore, van der Waals epitaxial VS growth was previously reported on special substrates such as mechanically exfoliated graphene,[24] boron nitride,[25] and cleaved fluorophlogopite mica ($[KMg_3(AlSi_3O_{10})F_2]$),[26] which have relatively small lattice mismatch with these TI materials. With this van der Waals epitaxy mechanism, vertical heterostructures were formed by growing the second material on top of an existing nanoplate.[24] Here, based on these van der Waals epitaxy substrates, we developed an *in situ* growth setup to achieve the synthesis of lateral heterostructures, in which the second material is in-plane adjoined to the layer edge dangling bond of the first material while epitaxial on the substrate.

RESULTS AND DISCUSSION

An *in situ* two-step strategy was developed for the preparation of lateral heterostructures. The whole synthesis process was carried out in a quartz tube under argon flow. Two source powders were sealed in the tube before the heat treatment process. In order to avoid breaking the vacuum, we developed a new method by using specially designed boats to exchange the positions of two sources between two growth steps. The growth order of the materials is determined by their melting point. The high melting point material is first grown, which reduces the amount of its residual evaporation during the growth of the second materials. As an example, we show the growth of Bi_2Te_3/Bi_2Se_3 heterostructures (Figure 1c). During the first growth, Bi_2Se_3 source powder was placed in a crucible boat in the hot center of the tube furnace, while the Bi_2Te_3 boat was left in the upstream cold zone. A freshly cleaved fluorophlogopite mica was used as a substrate and placed in the downstream cold zone. Bi_2Se_3 vapor is transported to the mica substrate by argon flow at the preset temperature to form Bi_2Se_3 nanoplates. The Bi_2Te_3 source powder is carried by a specially designed boat, which is higher in its vertical position than the Bi_2Se_3 boat and has an empty space under it, allowing the passing of the Bi_2Se_3 boat between two growths. After the first growth and natural cooling to lower than the Curie temperature of the magnet, we switched the positions of Bi_2Se_3 and Bi_2Te_3 sources using the quartz sealed magnet and performed the second growth to form Bi_2Te_3/Bi_2Se_3 lateral heterostructures.

In order to investigate the structure and composition of the as-synthesized Bi_2Te_3/Bi_2Se_3 heterostructures, scanning transmission electron microscopy (STEM) and energy-dispersive X-ray (EDX) mapping were performed. A low-magnification STEM image reveals that the product is composed of a plate-like nanoarchitecture (Figure 2a). Meanwhile, dark/light contrast is clearly observed at the edge of a nanoplate, suggesting the composition and/or structure differences. Furthermore, the EDX mapping characterizations were carried out, which provide composition distribution information over the structure. Clear composition contrast is shown in a selected edge area of the nanoplate. The Se signal is mainly observed in the inner region, while the Te signal only exists in the outer region of the nanoplate, which is consistent with the growth order. Note that the weak Se signal in the outer region arises from the interdiffusion of Se atoms from Bi_2Se_3 during the second growth. These results are compelling evidence for the successful synthesis of the lateral Bi_2Te_3/Bi_2Se_3 heterostructures with some Se outer diffusion. To show the versatility of our specially designed method to synthesize lateral heterostructures, the Bi_2Te_3/Sb_2Te_3 heterostructure was also successfully achieved *via* the same procedure but using Sb_2Te_3 as the source material for the first growth (Figure 2b).

To highlight the advances of our specially designed *in situ* synthesis method, we also characterized the Bi_2Te_3/Bi_2Se_3 heterostructures formed *via* an *ex situ* growth method (Supporting Information, Figure S1). The difference between these two methods is that the as-synthesized Bi_2Se_3 nanoplate in the *ex situ* growth method has to be exposed to the atmosphere due to the source change before the second step growth of Bi_2Te_3. As shown in Figure 2c, Bi_2Te_3/Bi_2Se_3 nanoplates

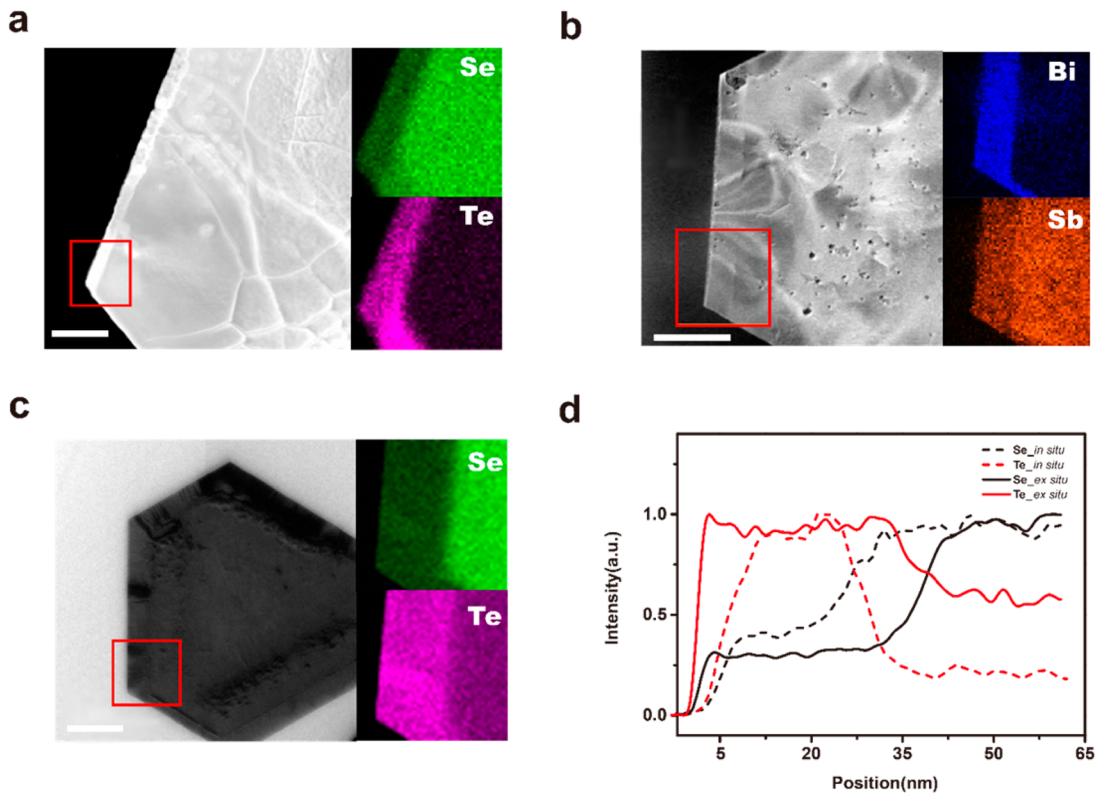

Figure 2. STEM and EDX mapping results of (a) *in situ* two-step synthesized Bi_2Te_3/Bi_2Se_3 heterostructure; (b) *in situ* two-step synthesized Bi_2Te_3/Sb_2Te_3 heterostructure, and (c) *ex situ* two-step synthesized Bi_2Te_3/Bi_2Se_3 heterostructure (scale bar 2 μm). (d) EDX line scan profiles across the interfaces of *in situ* and *ex situ* synthesized Bi_2Te_3/Bi_2Se_3 heterostructures. The Se intensity ratio of the inner and outer region is almost the same for *in situ* and *ex situ* synthesized heterostructures due to the diffusion of Se atoms. The Te intensity ratio of inner and outer regions of *in situ* synthesized heterostructures decreases significantly compared with the *ex situ* synthesized heterostructures, indicating the formation of a lateral heterostructure through the *in situ* synthesis process.

are also achieved *via* an *ex situ* synthesis process. Although a similar dark/light contrast is observed around the edge of the formed nanoplate under STEM, EDX mapping results show quite different composition distribution information. The most outstanding difference is that, in the inner region of this sample, we can easily identify the Te signal, which is not observed for the samples prepared *via* the specially designed *in situ* synthesis method. This phenomenon suggests the growth of a Bi_2Te_3 layer on top of the Bi_2Se_3 nanoplate for this controlled sample, while it is dramatically suppressed when the intermediate Bi_2Se_3 is not exposed to the atmosphere. A possible reason is that during the exposure of Bi_2Se_3 to the air, oxygen and water molecules are adsorbed on its surface, which creates the active sites and induces the nucleation and growth of Bi_2Te_3 on the basal planes of Bi_2Se_3 nanoplates. To qualify the composite distribution difference between the two Bi_2Te_3/Bi_2Se_3 heterostructures obtained from the *in situ* and *ex situ* synthesis methods, respectively, the EDX line scan across the interfaces was further investigated (Figure 2d). For the central areas and outer areas, Se signal ratios are almost the same for the two samples, indicating that diffusion of Se is not affected by the exposure to the ambient atmosphere. However, the ratio of Te signal at the inner region is dramatically suppressed without exposure to the atmosphere.

Understanding the growth mechanism of TI lateral heterostructures is important in determining their growth conditions of different steps and designing new device structures. AFM is an ideal technique for characterizing 2D nanomaterials such as Bi_2Se_3, Bi_2Te_3, and Sb_2Te_3 nanoplates,[23,24,26] due to its high resolution and minimal sample damage during characterization. In our experiment, *ex situ* AFM measurements were carried out to investigate the evolution of morphology and structure of these 2D heterostructures over their *ex situ* growth with air exposure between the two-step growth (Figure 3a). A Bi_2Se_3 nanoplate (obtained after the first growth for 10 min) is used as the base substrate, and Bi_2Te_3/Bi_2Se_3 heterostructures at different Bi_2Te_3 growth stages (2−8 min) were subject to AFM characterizations. Their morphology and structure information were collected and the growth mechanisms were analyzed. As shown in Figure 3b, after the first 2 min for Bi_2Te_3 growth, the lateral size of the nanoplate changes from 7.5 μm to 8.6 μm, and the AFM tip broadening effect only adds about 20 nm to the lateral size, which does not affect the lateral measurement

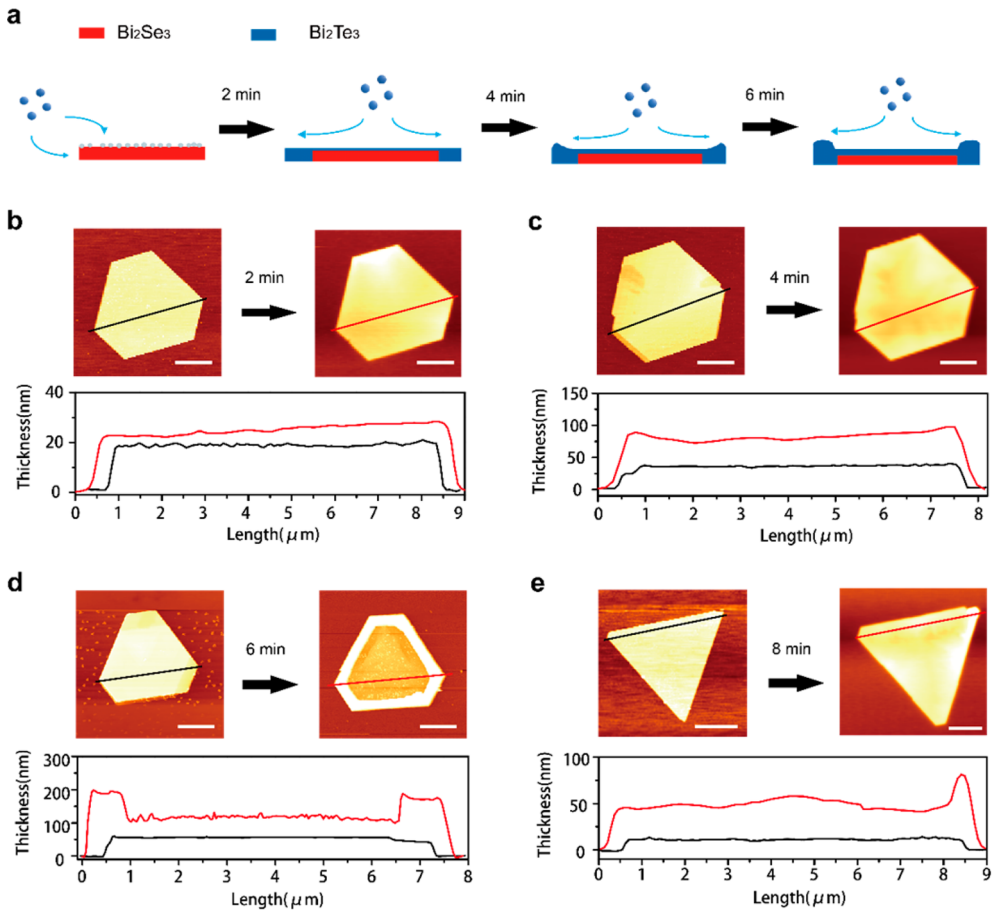

Figure 3. (a) Schematic of the growth mechanism for the air-exposed Bi_2Te_3/Bi_2Se_3 heterostructured nanoplate sample. Due to oxygen and water residue from the exposure to the ambient environment during AFM characterization, the second material (Bi_2Te_3) grew both laterally and on top of existing Bi_2Se_3 nanoplates. As the growth time increases, a crater structure will form on top of the original nanoplate, and the lateral growth starts to happen inside the crater. (b–e) *Ex situ* AFM measurement of the same nanoplates before and after the second step of growth. After (b) 2, (c) 4, (d) 6, and (e) 8 min of second-step growth, the nanoplates extend in both height and width. Height profiles show that a crater structure started to form after the second growth for 6 min (scale bar 2 μm).

accuracy in this much larger lateral size range. In contrast, the vertical thickness of the nanoplate increases only from 18 to 24 nm. Thus, with a high anisotropic ratio of ~100, the original nanoplate shows clear preferential growth in the horizontal plane as compared to the *z*-direction. The lateral growth of Bi_2Te_3 is due to the anisotropic bonding nature of these layered materials. Since Bi_2Se_3 and Bi_2Te_3 have similar lattice constants, incoming atoms tend to covalently bind to the dangling bonds around the edge of Bi_2Se_3 to form initial nuclei. After the nucleation, atomic growth continues at the edge site dangling bonds and leads to a higher growth rate in the lateral direction. Meanwhile, a thin layer of Bi_2Te_3 also forms on top of the Bi_2Se_3 nanoplates due to the oxygen and water residue from the exposure to the ambient environment during AFM characterization. As discussed above, without such exposure (*in situ* two-step growth), a very distinct lateral heterostructure can be obtained (Figure 2a). Once the top surface is terminated with chemically saturated Te atoms, vertical growth is slowed down and any adsorbed atoms tend to diffuse around to the edge sites. Verified by the two peaks at the edge in the AFM line scan for the samples with Bi_2Te_3 grown for 4 min, the edge of the nanoplate starts to grow thicker (Figure 3c) and further growth leads to the formation of a crater structure on top of the original nanoplate (Figure 3d). Since the protrusion at the edge has dangling bonds on both sides, the lateral growth also starts to happen inside the crater until it is filled (Figure 3e). This edge-induced growth mechanism is similar to the growth mechanism of few-layer Bi_2Te_3 and Bi_2Se_3 nanoplates resulting from their anisotropic bonding nature.[23] Control experiments were carried out to show that during the noncontact AFM measurements the probe would not contaminate the surface of the nanoplates (Supporting Information, Figure S2).

Our facile synthesis of various heterostructures with high quality paves the way for their advanced study in various fields. The as-obtained Bi_2Te_3/Bi_2Se_3 heterostructure consists of two n-type TIs, while the Bi_2Te_3/Sb_2Te_3 product is a topological p–n lateral heterostructure. It should be pointed out that some Sb atoms

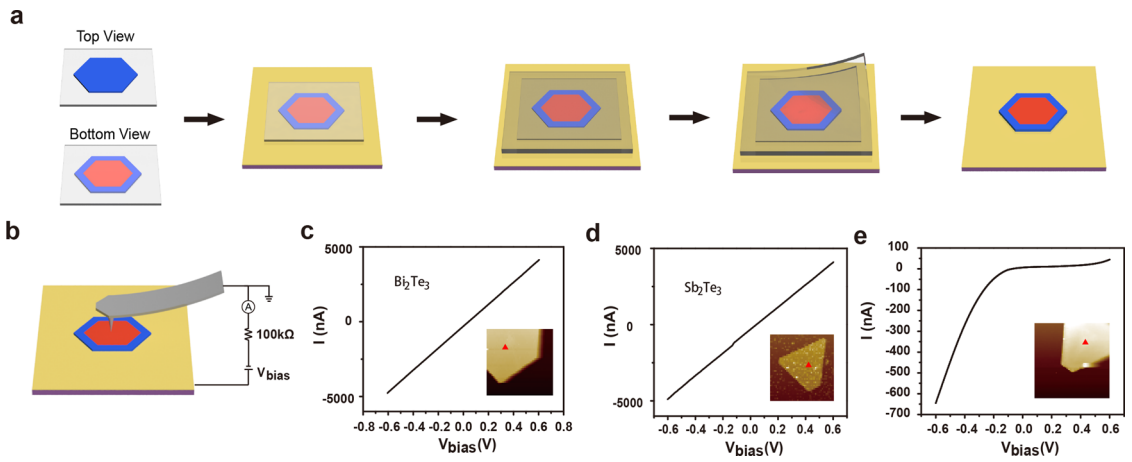

Figure 4. (a) Schematic of the clean transfer process to transfer the heterostructure from mica to a Au/Cr/silicon (10 nm/100 nm/300 μm) substrate and flip it over. (b) Schematic of the C-AFM measurement process. The sample is biased through the silicon substrate, while the AFM probe is grounded. (c, d) $I-V$ characteristics of Bi_2Te_3 and Sb_2Te_3 nanoplates. (e) $I-V$ characteristics of the Bi_2Te_3/Sb_2Te_3 heterostructure. The p−n diode rectification behavior demonstrates the existence of a p−n heterojunction.

diffuse into the Bi_2Te_3 area during the growth process of Sb_2Te_3 (Figure 2b) and form $(Bi_xSb_{1-x})_2Te_3$ alloy in the outer region of heterostructure. With different stoichiometry x, $(Bi_xSb_{1-x})_2Te_3$ alloy can be n-type or p-type.[22,27] However, in our experiment, this amount of Sb diffusion within the structure does not affect the p−n diode property of our sample. To confirm the existence of a p−n heterojunction, we carried out conductive AFM (C-AFM) measurements. To prepare the sample, we extend the *in situ* growth time of the second step to form a thick Bi_2Te_3 layer covering the whole Sb_2Te_3 nanoplate. Cross-section scanning electron microscopy (SEM) is carried out to show the structure of the sample (Supporting Information, Figure S3). Before the C-AFM characterization, we used a clean method to transfer sample from mica to a Au/Cr/silicon (10 nm/100 nm/300 μm) substrate. As shown in Figure 4a, a mica with sample on top is first flipped over and put on the Au/Cr/silicon substrate. Then it is covered by a 5 mm dry PDMS stamp and pressed slightly. Meanwhile, the silicon substrate is baked at 70 °C for 10 min to form van der Waals bonds between nanoplate samples and the Au layer. Finally, the PDMS stamp is lifted off carefully with the flipped heterostructured nanoplate sample left on the silicon substrate. By applying a small bias to the silicon substrate (Figure 4b), the topography and $I-V$ characteristics of the samples are simultaneously acquired by a Au/Cr-coated conductive AFM tip in contact C-AFM model. First, the $I-V$ characteristics of the Bi_2Te_3 nanoplate and Sb_2Te_3 nanoplate are obtained (Figure 4c,d). A linear $I-V$ relationship is observed for both the Bi_2Te_3 and Sb_2Te_3 nanoplate, indicating the metal contact barrier does not significantly affect the device behavior. The electrical transport study of the heterostructure shows clear current rectification behavior in the $I-V$ curve (Figure 4e), with current able to pass through the device only when the bottom n-type Bi_2Te_3 is negatively biased. The current rectification clearly demonstrates the existence of a p−n junction.

CONCLUSIONS

In summary, we have successfully demonstrated an *in situ* two-step synthesis process to grow TI lateral heterostructures on mica substrates. STEM images and EDX mappings show clear and sharp interfaces across the as-synthesized heterostructures, indicating high-quality 2D lateral heterostructures. AFM studies reveal the edge-activated growth mechanism for these TI lateral heterostructures. To prevent sample contamination, we develop a facile method to transfer samples from a mica substrate to a Au-coated silicon substrate. The existence of p−n junctions in the Bi_2Te_3/Sb_2Te_3 heterostructures is comfirmed by C-AFM measurements. The successful synthesis of a high-quality TI lateral heterostructure paves the way to create unprecedented TI electronics and spintronics.

METHODS

***In Situ* Two-Step Growth of Bi_2Te_3/Bi_2Se_3 Lateral Heterostructures.** The growth was carried out inside a one-inch-diameter quartz tube heated by a horizontal tube furnace (Lindberg/Blue M). Two quartz boats with different source powders, one quartz sealed magnet, and freshly cleaved fluorophlogopite mica substrates were put in the tube before the growth. The tube was then pumped to approximately 5 mTorr and flushed with ultrapure argon gas several times to remove oxygen residues. In the first growth step, the boat containing high melting point material Bi_2Se_3 (Alfa Aesar, purity 99.999%) was placed in the hot center of the tube furnace, while the boat with low melting point material Bi_2Te_3 (Alfa Aesar, purity 99.999%) was left in the

upstream cold zone. The mica substrates were placed in the downstream cold zone about 12 cm away from the center. During the growth, ultrapure argon (flow rate ~30 sccm) was used as a carrier gas to transport the source materials' vapor to the mica substrates. The growth pressure was set at ~900 mTorr with a growth temperature of ~490 °C and growth time of ~5 min. After the first growth, we used the quartz sealed magnet to switch the positions of Bi_2Se_3 and Bi_2Te_3 sources without breaking the vacuum. Then the furnace was heated to ~470 °C to perform the second growth to form Bi_2Te_3/Bi_2Se_3 lateral heterostructures. The Bi_2Te_3/Sb_2Te_3 lateral heterostructures can be achieved through the same procedure by changing the source powder of first growth step to Sb_2Te_3 (Alfa Aesar, purity 99.999%). For the *ex situ* two-step growth method, the as-synthesized Bi_2Se_3 nanoplate was exposed to the air atmosphere due to the source change before the second step growth of Bi_2Te_3.

Characterizations. AFM (Park Systems XE-70), SEM (FEI XL30 Sirion), STEM, and EDX mapping (FEI Tecnai G2 F20 X-TWIN) were carried out to characterize the samples. A carbon-film-supported copper grid was used for STEM characterization.

Electrical Transport Measurements of Bi_2Te_3/Sb_2Te_3 Heterostructures. The electrical transport studies were carried out by using conductive atomic force microscopy (Park Systems XE-100) with a conductive cantilever (Park Systems NSC18/Cr−Au). The C-AFM measurement was carried out under a sample-biased configuration with an external 100 kΩ resistance. Bi_2Te_3/Sb_2Te_3 heterostructure nanoplates were transferred to a Au/Cr/silicon (10 nm/100 nm/300 μm) substrate before the experiments.

Conflict of Interest: The authors declare no competing financial interest.

Acknowledgment. Y.C. acknowledges the support from the DARPA MESO project (no. N66001-11-1-4105). G.Z. acknowledges financial support from Agency for Science, Technology and Research (A*STAR), Singapore.

Supporting Information Available: The Supporting Information is available free of charge on the ACS Publications website at DOI: 10.1021/acsnano.5b04068.

Experimental details and additional figures (PDF)

REFERENCES AND NOTES

1. Geim, A. K.; Grigorieva, I. V. Van der Waals Heterostructures. *Nature* **2013**, *499*, 419–425.
2. Levendorf, M. P.; Kim, C.-J.; Brown, L.; Huang, P. Y.; Havener, R. W.; Muller, D. A.; Park, J. Graphene and Boron Nitride Lateral Heterostructures for Atomically Thin Circuitry. *Nature* **2012**, *488*, 627–632.
3. Liu, L.; Park, J.; Siegel, D. A.; McCarty, K. F.; Clark, K. W.; Deng, W.; Basile, L.; Idrobo, J. C.; Li, A.-P.; Gu, G. Heteroepitaxial Growth of Two-Dimensional Hexagonal Boron Nitride Templated by Graphene Edges. *Science* **2014**, *343*, 163–167.
4. Liu, Z.; Ma, L. L.; Shi, G.; Zhou, W.; Gong, Y. J.; Lei, S. D.; Yang, X. B.; Zhang, J. N.; Yu, J. J.; Hackenberg, K. P.; et al. In-plane Heterostructures of Graphene and Hexagonal Boron Nitride with Controlled Domain Sizes. *Nat. Nanotechnol.* **2013**, *8*, 119–124.
5. Gong, Y. J.; Lin, J. H.; Wang, X. L.; Shi, G.; Lei, S. D.; Lin, Z.; Zou, X. L.; Ye, G. L.; Vajtai, R.; Yakobson, B. I.; et al. Vertical and In-Plane Heterostructures from WS_2/MoS_2 Monolayers. *Nat. Mater.* **2014**, *13*, 1135–1142.
6. Huang, C.; Wu, S.; Sanchez, A. M.; Peters, J. J.P.; Beanland, R.; Ross, J. S.; Rivera, P.; Yao, W.; Cobden, D. H.; Xu, X. Lateral Heterojunctions within Monolayer $MoSe_2-WSe_2$ Semiconductors. *Nat. Mater.* **2014**, *13*, 1096–1101.
7. Duan, X. D.; Wang, C.; Shaw, J. C.; Cheng, R.; Chen, Y.; Li, H. L.; Wu, X. P.; Tang, Y.; Zhang, Q. L.; Pan, A. L.; et al. Lateral Epitaxial Growth of Two-Dimensional Layered Semiconductor Heterojunctions. *Nat. Nanotechnol.* **2014**, *9*, 1024–1030.
8. Yu, J. H.; Lee, H. R.; Hong, S. S.; Kong, D. S.; Lee, H.-W.; Wang, H. T.; Xiong, F.; Wang, S.; Cui, Y. Vertical Heterostructure of Two-Dimensional MoS_2 and WSe_2 with Vertically Aligned Layers. *Nano Lett.* **2015**, *15*, 1031–1035.
9. Moore, J. E. The Birth of Topological Insulators. *Nature* **2010**, *464*, 194–198.
10. Hasan, M. Z.; Kane, C. L. Colloquium: Topological Insulators. *Rev. Mod. Phys.* **2010**, *82*, 3045.
11. Qi, X.-L.; Zhang, S.-C. Topological Insulators and Superconductors. *Rev. Mod. Phys.* **2011**, *83*, 1057.
12. Xia, Y.; Qian, D.; Hsieh, D.; Wray, L.; Pal, A.; Lin, H.; Bansil, A.; Grauer, D.; Hor, Y. S.; Cava, R. J.; et al. Observation of a Large-Gap Topological-Insulator Class with a Single Dirac Cone on the Surface. *Nat. Phys.* **2009**, *5*, 398–402.
13. König, M.; Wiedmann, S.; Brüne, C.; Roth, A.; Buhmann, H.; Molenkamp, L. W.; Qi, X.-L.; Zhang, S.-C. Quantum Spin Hall Insulator State in HgTe Quantum Wells. *Science* **2007**, *318*, 766–770.
14. Qi, X.-L.; Zhang, S.-C. The Quantum Spin Hall Effect and Topological Insulators. *Phys. Today* **2010**, *63*, 33–38.
15. Bernevig, B. A.; Hughes, T. L.; Zhang, S.-C. Quantum Spin Hall Effect and Topological Phase Transition in HgTe Quantum Wells. *Science* **2006**, *314*, 1757–1761.
16. Fu, L.; Kane, C. L. Topological Insulators with Inversion Symmetry. *Phys. Rev. B: Condens. Matter Mater. Phys.* **2007**, *76*, 045302.
17. Zeng, Z.; Morgan, T. A.; Fan, D.; Li, C.; Hirono, Y.; Hu, X.; Zhao, Y.; Lee, J. S.; Wang, J.; Wang, Z. M.; et al. Molecular Beam Epitaxial Growth of Bi_2Te_3 and Sb_2Te_3 Topological Insulators on GaAs (111) Substrates: A Potential Route to Fabricate Topological Insulator p-n Junction. *AIP Adv.* **2013**, *3*, 072112.
18. Zhao, Y.; Chang, C.-Z.; Jiang, Y.; DaSilva, A.; Sun, Y.; Wang, H.; Xing, Y.; Wang, Y.; He, K.; Ma, X.; et al. Demonstration of Surface Transport in A Hybrid Bi_2Se_3/Bi_2Te3 Heterostructure. *Sci. Rep.* **2013**, *3*, 3060.
19. Seradjeh, B.; Moore, J. E.; Franz, M. Exciton Condensation and Charge Fractionalization in a Topological Insulator Film. *Phys. Rev. Lett.* **2009**, *103*, 066402.
20. Wang, J.; Chen, X.; Zhu, B.-F.; Zhang, S.-C. Topological p-n Junction. *Phys. Rev. B: Condens. Matter Mater. Phys.* **2012**, *85*, 235131.
21. Ilan, R.; de Juan, F.; Moore, J. E. *Spin-Based Mach-Zehnder Interferometry in Topological Insulator p-n Junctions*. **2014**, *arXiv:1410.5823.* arXiv.org e-Print archive. http://arxiv.org/abs/1410.5823 (accessed Oct 2014).
22. Kong, D. S.; Chen, Y. L.; Cha, J. J.; Zhang, Q. F.; Analytis, J. G.; Lai, K. J.; Liu, Z. K.; Hong, S. S.; Koski, K. J.; Mo, S.-K.; et al. Ambipolar Field Effect in the Ternary Topological Insulator $(Bi_xSb_{1-x})_2Te_3$ by Composition Tuning. *Nat. Nanotechnol.* **2011**, *6*, 705–709.
23. Kong, D. S.; Dang, W. H.; Cha, J. J.; Li, H.; Meister, S.; Peng, H. L.; Liu, Z. F.; Cui, Y. Few-Layer Nanoplates of Bi_2Se_3 and Bi_2Te_3 with Highly Tunable Chemical Potential. *Nano Lett.* **2010**, *10*, 2245–2250.
24. Dang, W. H.; Peng, H. L.; Li, H.; Wang, P.; Liu, Z. F. Epitaxial Heterostructures of Ultrathin Topological Insulator Nanoplate and Graphene. *Nano Lett.* **2010**, *10*, 2870–2876.
25. Gehring, P.; Gao, B. F.; Burghard, M.; Kern, K. Growth of High-Mobility Bi_2Te_2Se Nanoplatelets on hBN Sheets by Van der Waals Epitaxy. *Nano Lett.* **2012**, *12*, 5137–5142.
26. Li, H.; Cao, J.; Zheng, W. S.; Chen, Y. L.; Wu, D.; Dang, W. H.; Wang, K.; Peng, H. L.; Liu, Z. F. Controlled Synthesis of Topological Insulator Nanoplate Arrays on Mica. *J. Am. Chem. Soc.* **2012**, *134*, 6132–6135.
27. Zhang, J. S.; Chang, C.-Z.; Zhang, Z. C.; Wen, J.; Feng, X.; Li, K.; Liu, M. H.; He, K.; Wang, L. L.; Chen, X.; et al. Band Structure Engineering in $(Bi_{1-x}Sb_x)_2Te_3$ Ternary Topological Insulators. *Nat. Commun.* **2011**, *2*, 574.